

Fit-sphere unwrapping and performance analysis of 3D fingerprints

Yongchang Wang, Daniel L. Lau,* and Laurence G. Hassebrook

1 Quality Street Suite 800, University of Kentucky, Lexington, Kentucky, 40507, USA

*Corresponding author: dllau@engr.uky.edu

Received 21 September 2009; revised 5 November 2009; accepted 8 December 2009;
posted 15 December 2009 (Doc. ID 117492); published 25 January 2010

To solve problems associated with conventional 2D fingerprint acquisition processes including skin deformations and print smearing, we developed a noncontact 3D fingerprint scanner employing structured light illumination that, in order to be backwards compatible with existing 2D fingerprint recognition systems, requires a method of unwrapping the 3D scans into 2D equivalent prints. For the latter purpose of virtually flattening a 3D print, this paper introduces a fit-sphere unwrapping algorithm. Taking advantage of detailed 3D information, the proposed method defuses the unwrapping distortion by controlling the distances between neighboring points. Experimental results will demonstrate the high quality and recognition performance of the 3D unwrapped prints versus traditionally collected 2D prints. Furthermore, by classifying the 3D database into high- and low-quality data sets, we demonstrate that the relationship between quality and recognition performance holding for conventional 2D prints is achieved for 3D unwrapped fingerprints. © 2010 Optical Society of America

OCIS codes: 100.5010, 100.2960, 100.6890, 070.6110, 110.6880.

1. Introduction

Fingerprints are the friction ridge and furrow patterns on the finger that have been extensively applied in both forensic law enforcement and security applications [1–4]. But the acquisition, analysis, and recognition of fingerprints are still considered by many experts to be an active area of research [5–10]. Traditional fingerprint images are acquired by pressing or rolling a finger against a hard surface (e.g., prism, silicon, polymer, index card) [7,11,12]; however, these contact-based applications often result in low-quality prints [8,13–17] due, mainly, to the uncontrollability and nonuniformity of finger pressure as well as from residues from the previous fingerprint.

To eliminate these drawbacks of traditional 2D scanning, noncontact fingerprint scanners have been developed that include a broad set of 3D scanners [8,14,18–21]. Since direct contact between sensor and finger skin is avoided, these noncontact sensors

consistently preserve the fingerprints ground truth and achieve higher recognition performance. Among these scanners, the TBS (Touchless Biometric Systems) multicamera touchless fingerprint system developed in [19] acquires different finger views that are subsequently merged to form a wraparound 3D fingerprint. In this system, the shape of the finger is acquired by using the shape-from-silhouette technique without contact between the elastic skin of the finger and any rigid surface. Thus, the deformation of prints is greatly reduced.

Ridge information, in the TBS system, is extracted from the finger surface reflection variation (albedo), where, to be compatible with the legacy rolled fingerprint images used in automated fingerprint identification systems, the 3D touchless prints are unwrapped into 2D ones [22]. The unwrapping algorithm tries to unfold the 3D prints in such a way that it resembles the effect of virtually rolling the 3D on a 2D plane [22]. The drawback of using the shape-from-silhouette technique is that only the shape of the finger is obtained, without the detailed 3D ridge information. Thus, the distortion caused by the unwrapping algorithm is difficult to control, and since

the ridge information is extracted from texture data, the obtained prints could be affected by surface color, surface reflectance, and geometric factors as well as other imaging effects.

In [23], we presented an alternative approach to 3D fingerprint scanning using structured light illumination. Different from the system in [19], our system acquires the detailed 3D information such that the ridge information can be obtained from the surface geometry instead of the albedo. Many degrading factors from the nonuniform surface conditions have been overcome, and to be compatible with conventional 2D prints, a springs-inspired algorithm was developed [24] for unwrapping the 3D scans. This algorithm was based upon a web of virtual springs spanning the fingerprint surface, where, first, ridges were extracted from the surface. The remaining 3D points were then treated as a mechanical system in which points had mass, and these points of mass were interconnected by means of mechanical springs. The mesh was then pressed down onto a flat plane. As a nonparametric method, the computational cost of the springs algorithm was high.

To reduce the computational cost and the distortion caused by the springs unwrapping process, this paper introduces a fit-sphere algorithm that is based on best fitting a sphere to the 3D surface and then mapping the original 3D points clouds, stored in Cartesian coordinates, to spherical coordinates (θ, ϕ, ρ) . Since the detailed 3D information is available for each point (pixel), the initial linear unwrapping mesh (θ, ϕ) will be resampled to be nonlinear such that the distance among neighboring pixels matches the required resolution (500 ppi) of 2D prints. Finally, after mapping to spherical coordinates, fingerprint ridges will be extracted from depth by applying a bandpass filter to the ρ dimension, where the low-frequency, smooth contours of the finger surface as well as the high-frequency, noise fluctuations will be removed. Since this algorithm is developed from parametric unwrapping methods, the computational cost is reduced compared with the springs algorithm, and by taking advantage of detailed 3D information, the unwrapping based on the nonlinear mesh achieves less deformation.

To evaluate the quality of the resulting 2D equivalent prints, this paper will use the quality analysis metrics originally tested in [23], which will be applied to the 3D unwrapped fingerprints. For comparison, we will apply the same metrics to the equivalent prints produced using the recognition algorithm developed by National Institute of Standards and Technology (NIST). Experimental results will show that the unwrapped prints produced by our technique achieve high recognition performance. Furthermore, by classifying the 3D scans into either high- and low-quality data sets and performing matching within and between the two sets, we will show that high-quality 3D unwrapped prints achieve a higher recognition performance than the low-quality ones. Thus, we will demonstrate the relation-

ship between quality and recognition performance, holding for 2D prints, is also true for the 3D unwrapped ones—lending credence to the theory that the NIST image quality metrics are indicators of matching performance when one lacks large-scale databases by which matching performance can be adequately evaluated.

We present a brief description of the 3D data acquisition procedures in Section 2. Section 3 introduces the fit-sphere algorithm, while in Section 4, we perform both analyze scan quality and recognition-matching performance, demonstrating that the relationship between quality and recognition performance for conventional 2D prints also applies to 3D unwrapped prints. The conclusions and future work is presented in Section 5.

2. 3D Fingerprint Acquisition

The 3D fingerprint prototype was developed by Flashscan 3D LLC and the University of Kentucky using multipattern, phase-measuring profilometry (PMP), shown in Fig. 1 and described in [25–27]. Compared with other methods of 3D range sensing such as stereo vision and laser scanning, multipattern structured light illumination has the advantage of being low cost, having fast data acquisition and processing, and achieving high accuracy with dense surface reconstructions [25]. PMP or the sinusoidal fringe pattern, in particular, is employed because of its high efficiency and robustness to defocus [26,28].

In PMP, the series of N sinusoidal light patterns, projected onto the target surface is expressed as [29]

$$I_n^p(x^p, y^p) = A^p + B^p \cos \left[\varepsilon(x^p, y^p) + \frac{2\pi n}{N} \right], \quad (1)$$

where x^p and y^p are two constants of the projector and $2\pi n/N$ is the shifted phase of the N patterns. The term $\varepsilon(x^p, y^p)$ is the phase of the current pixel, assigned as

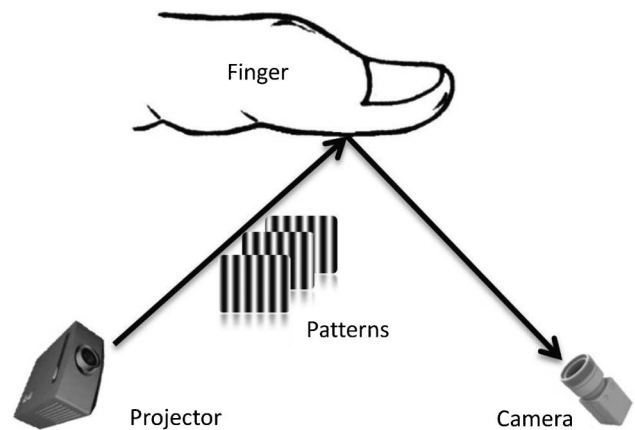


Fig. 1. Noncontact 3D fingerprint acquisition using the PMP technique.

$$\varepsilon(x^p, y^p) = \frac{2\pi f y^p}{L}, \quad (2)$$

where L is the length of the pattern and f is the frequency of the sinusoidal signal. From the viewpoint of the camera, the received image is distorted by the target surface topology and is expressed as [26]

$$I_n^c(x^c, y^c) = A^c(x^c, y^c) + B^c(x^c, y^c) \cos \left[\varepsilon(x^c, y^c) + \frac{2\pi n}{N} \right]. \quad (3)$$

The term $\varepsilon(x^c, y^c)$ represents the phase of the signal at point (x^c, y^c) and can be obtained, if $N \geq 3$, as

$$\begin{aligned} \varepsilon(x^c, y^c) &= \arctan \left[\frac{U(x^c, y^c)}{V(x^c, y^c)} \right] \\ &= \arctan \left\{ \frac{\sin[\varepsilon(x^p, y^p)]}{\cos[\varepsilon(x^p, y^p)]} \right\}, \end{aligned} \quad (4)$$

where

$$U(x^c, y^c) = \sum_{n=1}^N \left[I_n^c(x^c, y^c) \sin \left(\frac{2\pi n}{N} \right) \right], \quad (5)$$

$$V(x^c, y^c) = \sum_{n=1}^N \left[I_n^c(x^c, y^c) \cos \left(\frac{2\pi n}{N} \right) \right]. \quad (6)$$

For high-frequency PMP patterns, the phase $\varepsilon(x^c, y^c)$ obtained from Eq. (4) is unwrapped into $[0, 2\pi f)$ [30]. Thus, from Eq. (2), the projector coordinate y^p can be recovered as

$$y^p(x^c, y^c) = \frac{\varepsilon(x^c, y^c)L}{2\pi f}. \quad (7)$$

The 3D information is computed from the precalibrated triangulation [27].

Further, the term $B^c(x^c, y^c)$ in Eq. (3) is computed as

$$B^c(x^c, y^c) = \frac{2}{N} [U^2(x^c, y^c) + V^2(x^c, y^c)]^{1/2}, \quad (8)$$

such that $B^c(x^c, y^c)$ can be thought of as the amplitude of the sinusoid reflecting off of a point on the target surface. So, it is used to remove the shadow noise and extract the fingerprint from the background. In practice, our system projects ten high-frequency PMP patterns to acquire 3D data. The resolution of the camera is 1392 pixels \times 1040 pixels ($H \times W$). An example 3D fingerprint is shown in Fig. 2, which displays several different views of the obtained 3D print. The width of the 3D print is about 850 points, and the height is about 1170 points. Depending on the depth, the lateral spacing

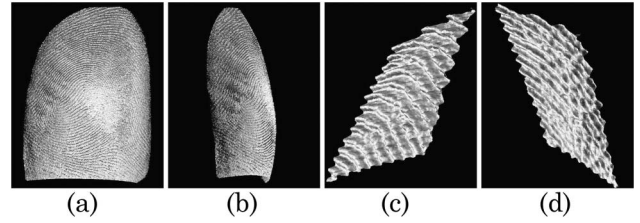


Fig. 2. (a) Front view of a 3D fingerprint. (b) Side view of the 3D print. (c), (d) Cropped and rotated piece of the 3D print. The 3D data is shown with depth rendering. The full fingerprint area spans approximately 21 mm \times 27 mm with point spacing between 20 and 25 μ m.

between points varies from 20 to 25 μ m. Most of the camera's field of view was occupied by the finger surface. Currently the system takes 0.7 s to scan a finger. So, to minimize the effects of finger movement and depth of focus, the fingernail rests against a support.

3. 3D Fingerprint Unwrapping

Creating a flattened print from the 3D scan requires the processing steps of (1) fitting a sphere to the scanned point cloud, (2) creating linear unwrapping maps, (3) correcting for distortion, and (4) extracting ridges.

A. Sphere Fitting

A sphere can be defined by specifying a center point (x^c, y^c, z^c) and radius r . The distance between a point on the print surface and a point on the sphere surface is obtained as

$$d = [(x_k - x^c)^2 + (y_k - y^c)^2 + (z_k - z^c)^2]^{1/2} - r, \quad (9)$$

where (x_k, y_k, z_k) is a point on the 3D print. For a 3D print with a total of K points ($K > 4$), Eq. (9) can be solved by the least squares fitting algorithm [31]. The sphere center point (x^c, y^c, z^c) and radius r are then obtained.

Now, to ensure that the unwrapping process is started from the center of the print, we choose to adjust the coordinates such that the north pole of the sphere (z axis) is coming out from the center of the scanned print. To do so, the coordinates of the points on the prints are changed to

$$x_k = x_k - x^c - \frac{\sum_{g=1}^{g=K} (x_g - x^c)}{K}, \quad (10)$$

$$y_k = y_k - y^c - \frac{\sum_{g=1}^{g=K} (y_g - y^c)}{K}, \quad (11)$$

$$z_k = z_k - z^c. \quad (12)$$

The point cloud is then translated in Cartesian space such that the center of the sphere is mapped to $(0, 0, 0)$. The Cartesian coordinates (x_k, y_k, z_k) are then converted to spherical coordinates $(\theta_k, \phi_k, \rho_k)$, where θ_k and ϕ_k are in units of radians, and ρ_k is

the distance from the center of the sphere to the k th point on the print surface.

B. Linear Unwrapping Maps

The unwrapping mesh consists of a θ and ϕ map, where the two linear θ and ϕ maps are created according to

$$\theta_{l_1}^{\text{linear}} = (l_1 - 1)t_\theta + \theta_{\min}, \quad (13)$$

$$\phi_{l_2}^{\text{linear}} = (l_2 - 1)t_\phi + \phi_{\min}, \quad (14)$$

where $l_1 = 1, 2, \dots, L_1$ and $l_2 = 1, 2, \dots, L_2$. The terms L_1 and L_2 are the height and width of the maps in pixels. The term θ_{\min} is the minimum value in $\{\theta_k\}$, ϕ_{\min} is the minimum value in $\{\phi_k\}$, and t_θ and t_ϕ are the step values assigned as

$$t_\theta = \min(|\theta_{w-1}^{\text{mean}} - \theta_w^{\text{mean}}|), \quad (15)$$

$$t_\phi = \min(|\phi_{h-1}^{\text{mean}} - \phi_h^{\text{mean}}|), \quad (16)$$

where θ_w^{mean} is the mean of θ values in the same row of the fingerprint scan and ϕ_h^{mean} is the mean of ϕ values in the same column. Thus,

$$L_1 = \frac{\max(\theta_k) - \min(\theta_k)}{t_\theta}, \quad (17)$$

$$L_2 = \frac{\max(\phi_k) - \min(\phi_k)}{t_\phi} \quad (18)$$

with the points in the same column of the θ map having the same value and the points in the same row of the ϕ map having the same value. Examples of the linear θ and ϕ maps are shown in Fig. 3, where $L_1 = 1200$ and $L_2 = 960$. The print is upsampled during linear unwrapping to preserve information. For each point (l_1, l_2) on the two maps, the mesh value is $(\theta_{l_1}^{\text{linear}}, \phi_{l_2}^{\text{linear}})$. The corresponding value of ρ_{l_1, l_2} is ob-

tained from bilinear interpolation to the 3D fingerprint $(\theta_k, \phi_k, \rho_k)$.

After obtaining the linear θ , linear ϕ , and ρ maps, we define the distance between two horizontal (along the L_1 direction) neighboring points as

$$d_{l_1}^\theta = |\theta_{l_1+1} - \theta_{l_1}| \frac{\rho_{l_1+1} + \rho_{l_1}}{2} \quad (19)$$

and the distance between two vertical (along the L_2 direction) neighboring points as

$$d_{l_2}^\phi = |\phi_{l_1+1} - \phi_{l_1}| \frac{\rho_{l_1+1} + \rho_{l_1}}{2}. \quad (20)$$

The distances along a horizontal line are plotted in Fig. 4, where the high-frequency wave is due to the ridges, while the lower-frequency curve of the cross section indicates that distortion exists in the ρ map.

C. Distortion Correction and Ridge Extraction

To defuse the distortion and scale the image to the required resolution, we create nonlinear θ and ϕ maps to achieve our desired resolution of 500 ppi where the distance between two neighboring points should be around $D = 0.0508$ mm. To reduce the noise in the ρ map, we first apply a low-pass filtering by means of a 15×15 Gaussian filter kernel with $\sigma = 5$. Then, we resize the linear θ map along the horizontal direction. The map is scaled from $L_1 \times L_2$ to $J_1 \times L_2$. The middle line of the linear map is filled into the center of the scaled map such that $\theta_{J_1/2} = \theta_{L_1/2}$. For the points in the left-hand part of the nonlinear map, the neighboring two points have

$$D = (\theta_{j_1-1} - \theta_{j_1}) \frac{\rho_{j_1}^{\text{lp}} + \rho_{j_1-1}^{\text{lp}}}{2}, \quad (21)$$

where $\rho_{j_1}^{\text{lp}}$ and $\rho_{j_1-1}^{\text{lp}}$ denote the low-pass filtered ρ map. To reduce the computational cost, we take $\rho_{j_1-1}^{\text{lp}} \approx \rho_{j_1}^{\text{lp}}$. Thus, the values of ρ^{lp} are further low-pass filtered, and

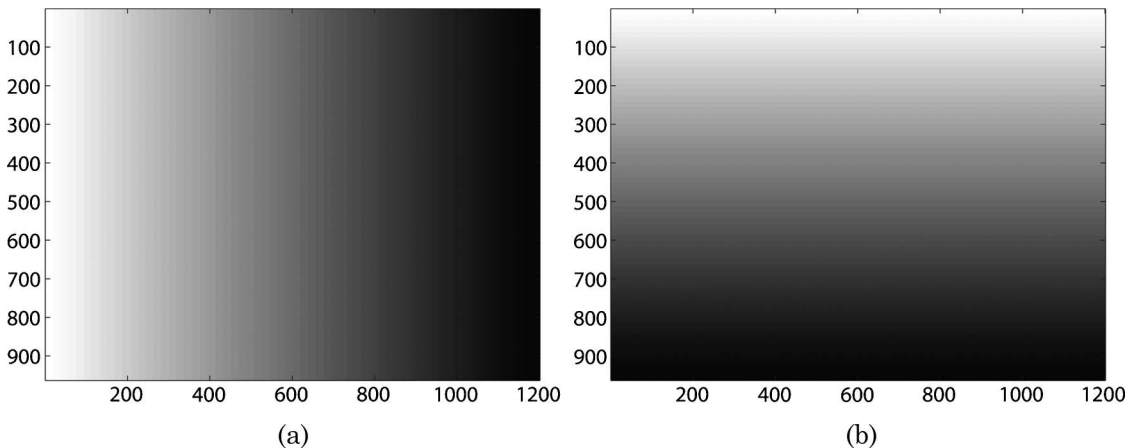


Fig. 3. (a) Linear θ map. (b) Linear ϕ map. The linear maps' width (pixels) $L_1 = 1200$, and the height (pixels) $L_2 = 960$.

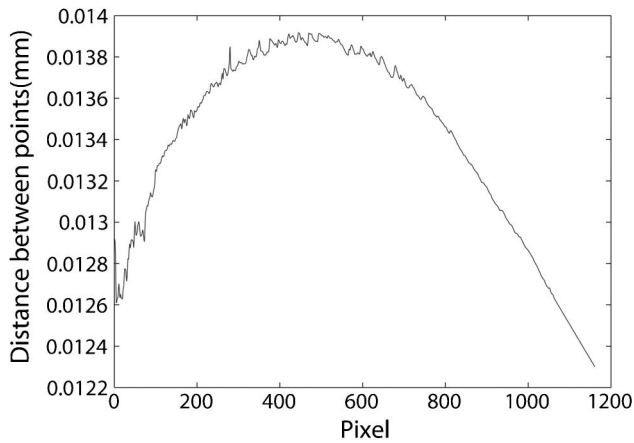


Fig. 4. Distance cross section of the upsampled print along the horizontal (θ) direction; linear unwrapping.

$$\theta_{j1-1} = \theta_{j1} + \frac{D}{\rho_{j1}^{\text{lp}}}. \quad (22)$$

For the points in the right-hand part of the nonlinear map, the θ values spread from middle to right such that

$$\theta_{j1+1} = \theta_{j1} - \frac{D}{\rho_{j1}^{\text{lp}}}. \quad (23)$$

With the resized θ map, the ϕ map is correspondingly resized to $J_1 \times L_2$ by linear interpolation. Similarly, we resize the ϕ map to $J_1 \times J_2$, with $\phi_{J_2/2} = \phi_{L_2/2}$, such that

$$\begin{aligned} \phi_{j2-1} &= \phi_{j2} + \frac{D}{\rho_{j2}^{\text{lp}}} & \text{if } j2 < \frac{J_2}{2}, \\ \phi_{j2+1} &= \phi_{j2} - \frac{D}{\rho_{j2}^{\text{lp}}} & \text{if } j2 > \frac{J_2}{2}. \end{aligned} \quad (24)$$

So through the above procedures, the linear θ and ϕ maps in Fig. 3 will no longer be linear; the nonlinear maps are shown in Fig. 5. Based on the nonlinear

maps, the 3D fingerprint is unwrapped from the 3D scan $(\theta_k, \phi_k, \rho_k)$ by bilinear interpolation.

So while the nonlinear maps distort the θ and ϕ values, they also minimize distortion during unwrapping of the 3D fingerprints where the distance between two neighboring points [Eqs. (19) and (20)], either along the horizontal or vertical direction, will be close to 0.0508 mm. The print is downsampled during the nonlinear unwrapping to achieve the required resolution of 500 ppi. As is seen from Fig. 6, the distortion in Fig. 4 is reduced, and the ridge information is preserved (the high-frequency wave). Further, we implement bandpass filtering by means of a 12×12 Gaussian low-pass filter with $\sigma^{\text{lp}} = 4$ followed by a 6×6 Gaussian high pass filter with $\sigma^{\text{hp}} = 2$. The filtered image is histogram equalized for final result. The unwrapped result is shown in Fig. 7.

4. Experimental Results and Discussion

For the purpose of quality and recognition performance analysis, a 3D fingerprint database was created by using the 3D fingerprint prototype at the University of Kentucky, and a 2D traditional ink rolled fingerprint database was collected by a trained operator at the University of Kentucky's campus police department. The 3D database consists of 450 prints from 30 index fingers, where each finger was scanned 15 times. All fingers were scanned by using the 3D fingerprint scanner described in Section 2. The camera resolution of the scanner was 1392 pixels \times 1040 pixels ($H \times W$), where, depending on the depth, the lateral spacing between points typically varies from 20 to 25 μm . The obtained 3D fingerprints were further unwrapped by the fit-sphere algorithm, which unwrapped and downsampled the 3D prints to the unwrapped prints with resolution of 500 ppi. The 2D print database has 150 prints from 15 different subjects (persons) with each of their 10 fingers rolled once. The resolution of the 2D prints is also 500 ppi.

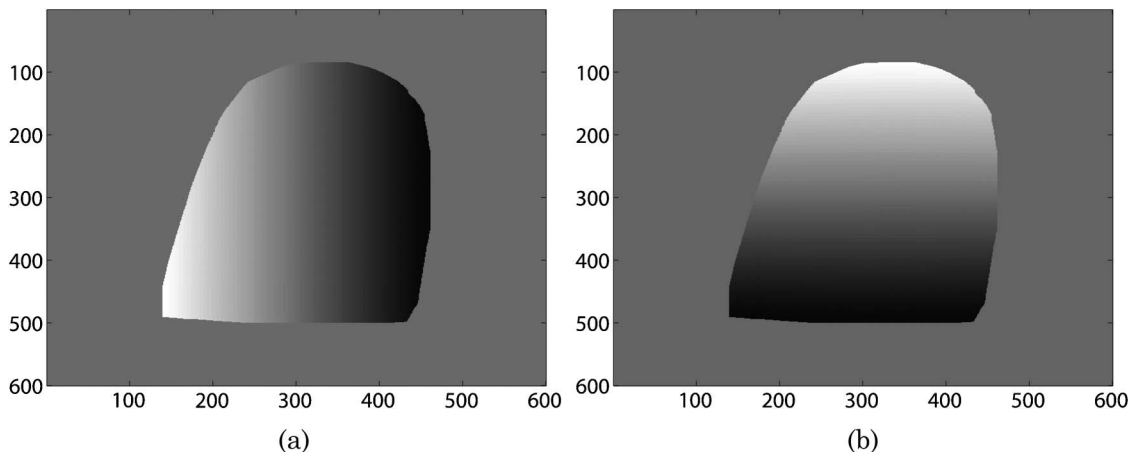


Fig. 5. (a) Nonlinear θ map. (b) Nonlinear ϕ map. The nonlinear maps' width (pixels) $J_1 = 600$, and the height (pixels) $J_2 = 600$.

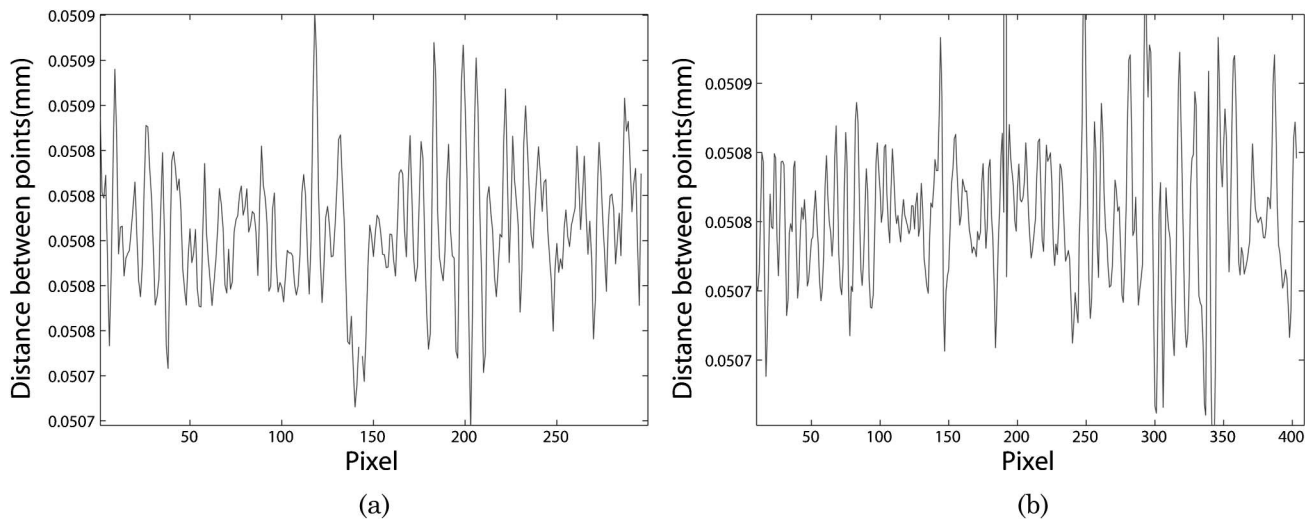


Fig. 6. (a) Distance cross section of the downsampled print along the horizontal (θ) direction; nonlinear unwrapping. (b) Distance cross section of the downsampled print along the vertical (ϕ) direction; nonlinear unwrapping.

A. Quality Analysis

To assess quality, we rely on the NIST Fingerprint Image Software (NFIS) [32]. As we shown in [23], out of the 11 identified metrics, 4 were found to be most suitable for evaluating quality: (1) local image quality, (2) minutiae quality, (3) classification confidence number, and (4) overall image quality number. In particular, a superior scanning technology should generate more blocks with high local quality (zone 4 representing the highest local quality), a higher number of reliable minutiae (greater than 20), a higher confidence number on classification, and a

lower overall image quality number (1 representing the highest overall quality).

With regard to local image quality scores, NFIS divides the input images into blocks with 8×8 pixels in each block and assigns a local quality number to the block with quality zone 4 representing the highest local quality [32]. Figure 8(a) shows that both 3D and 2D follow a similar trend, decreasing in the percentage of quality zone 4 blocks with increasing overall quality number. For prints with the same overall quality numbers, the 3D unwrapped prints achieve a higher percentage of quality zone 4 than that do 2D ink rolled prints. The 3D prints outperform the 2D ones in local quality analysis.

As for minutiae points, these features are widely used for fingerprint verification [9,16]. The NFIS system takes a fingerprint image and locates all the minutiae in the image, assigning to each minutiae point its location, orientation, and type. NFIS also calculates the quality and reliability of the detected minutiae with a confidence score that ranges from 0.0 to 1.0. Minutiae with quality greater than 0.75 are regarded as high quality. Tabassi *et al.* [32] observed that, generally, if a fingerprint has more than 20 of these high-quality minutiae, it would be more likely to be identified correctly by fingerprint recognition systems. From Fig. 8(b), it can be seen that, again, the trends of high-quality minutiae are similar for both data sets from quality numbers 1 to 5. For the same quality number prints, more high-quality (>75%) minutiae are detected in the 3D set than in the 2D set.

Our third metric, classification of the fingerprint pattern, is important for improving recognition speed. The NFIS system classifies the prints into basic pattern-level classes of (1) arch; (2) left loop; (3) right loop; (4) scar; (5) tented arch; or (6) whorl, along with a confidence number ranging from 0.0 to 1.0, where 1.0 represents the highest confidence of classification. Figure 8(c) indicates that in quality



Fig. 7. The final 3D unwrapped fingerprint downsampled to 500 ppi. The width of the resulting image is 450 pixels, and the height is 510 pixels.

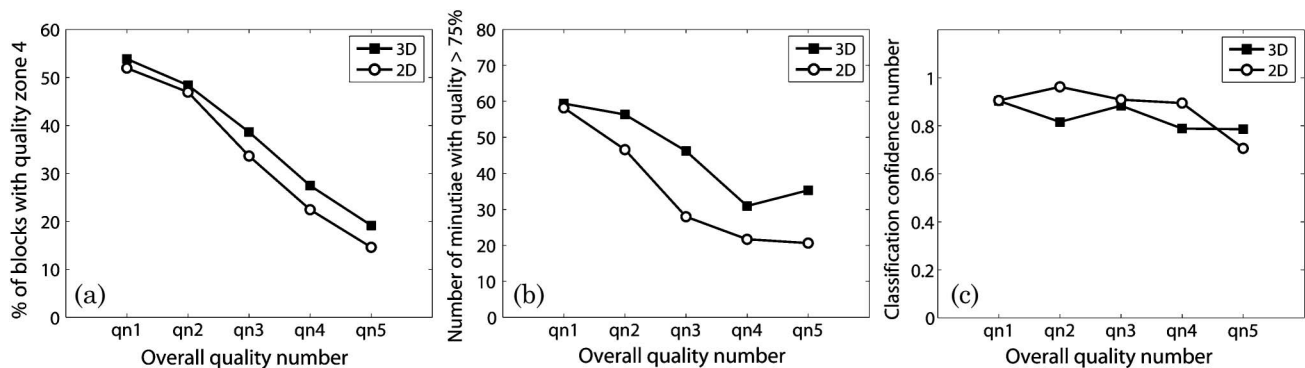


Fig. 8. (a) Percentage of blocks in quality zone 4, which is highest local quality zone, with respect to different overall quality numbers. (b) Number of minutiae with quality greater than 0.75, with respect to different overall quality numbers. (c) Classification confidence number, with respect to different overall quality numbers.

numbers 1 and 3, the 2D and 3D sets achieve the same or close performance in classification confidence, while in quality numbers 2 and 4, the 2D performs better than the 3D. 3D outperforms 2D in quality number 5. However, as shown in Fig. 8(c), either 3D or 2D is stably increasing or decreasing with increasing overall quality number. Thus, 3D unwrapped fingerprints achieve a higher quality than 2D ink rolled fingerprints in local quality and minutiae detection. Compared with the springs algorithm [24], the quality of the 3D unwrapped prints is improved.

B. Recognition Performance

In this section, recognition performance of 3D prints is studied. While many matching algorithms have been developed [10,33,34], we will focus on the BOZORTH3 system included in the NFIS package. It employs features to minutiae of the fingerprints, and produces a real-valued similarity score. The higher the score is, the more likelihood that the two fingers are from the same finger of the same subject. If the input of two fingerprints are actually from the same finger, then we refer to the score as a genuine score [6]; otherwise, it is noted as impostor score

[6], if the two fingerprints are from the same finger but of different subjects. For each pair of two fingerprints that are from the same finger of the same subject, we obtain one genuine score, with our database producing 3,150 genuine scores. Correspondingly, each fingerprint is matched with nonmatching fingerprints (the same finger of different subjects) where the other fingerprints are randomly selected. For this study, we will match the number of genuine scores with 3,150 impostor scores.

Looking at the histograms of genuine and impostor scores, there should, ideally, be no overlap between the two histograms, with genuine scores having higher value than impostor; however, in practice, overlap exists. As seen in Fig. 9, there is some amount of overlap between the genuine and impostor scores; furthermore, based on the distributions, we derive the receiver operating characteristic (ROC) in Fig. 10, which is a statement of the performance of the fingerprint verification system [6,16,35–37]. The false accept rate (FAR) and true accept rate (TAR) values are computed at each operating threshold. For a generally specific FAR, 0.1, the TAR for our system achieves 0.988.

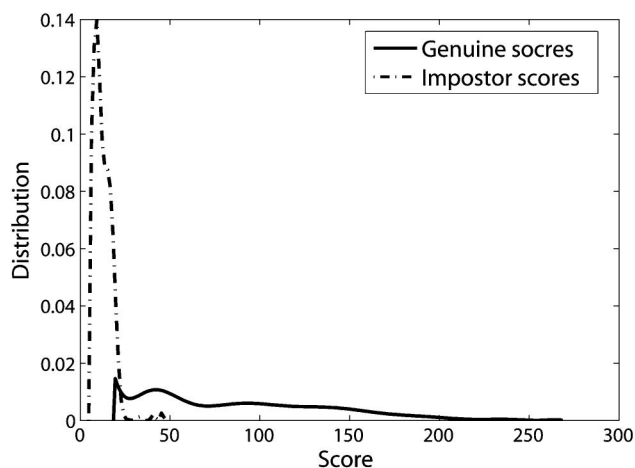


Fig. 9. Distributions of genuine and impostor scores for 3D unwrapped fingerprints.

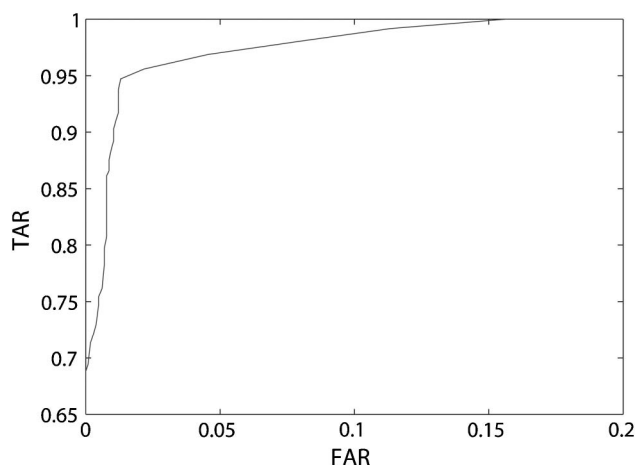


Fig. 10. ROC of 3D unwrapped fingerprints, TAR versus FAR.

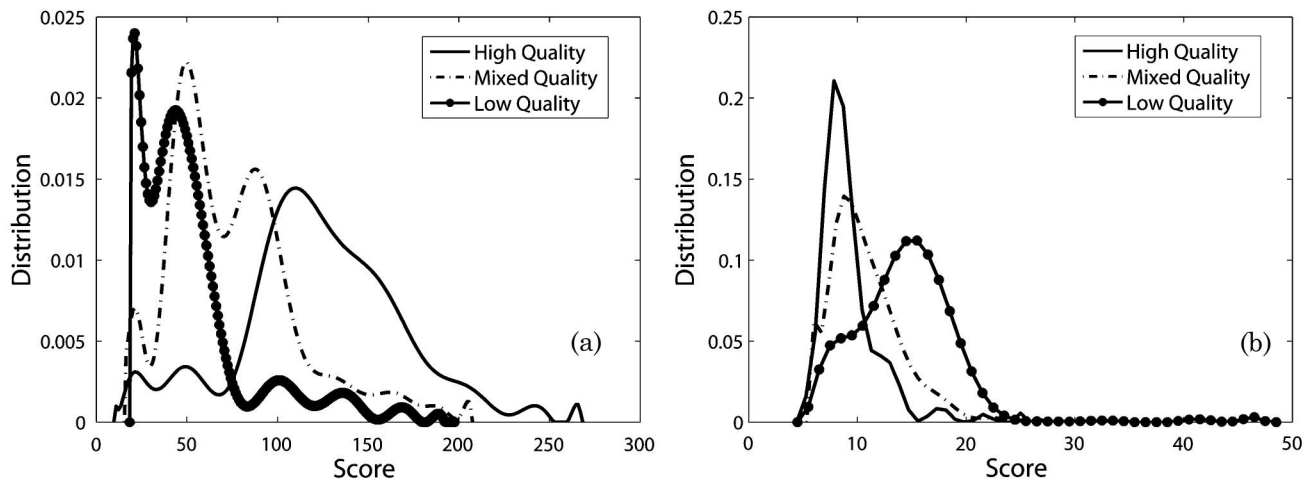


Fig. 11. (a) Distributions of genuine scores for the high-, mixed-, and low-quality matchings for 3D unwrapped fingerprints. (b) Distributions of impostor scores for the high-, mixed-, and low-quality matchings for 3D unwrapped fingerprints.

C. Relationship between Quality and Recognition Performance

For 2D fingerprints, the higher quality the print is, the higher recognition performance the print is expected to achieve. In order to study the relationship between quality and recognition performance for 3D unwrapped fingerprints, we divide the 3D database into two groups: high (if the overall quality number is 1 or 2) and low (if the overall quality number is 3, 4 or 5) quality groups. The recognition is regarded as high quality matching if the two matched prints are both high quality, regarded as mixed quality matching if one print is high quality and the other is low quality, and regarded as low quality matching if both prints are low quality. Totally, we have 910 high quality matchings, 1,260 mixed quality matchings, and 980 low quality matchings.

Figure 11(a) shows the genuine scores for high-, mixed-, and low-quality matchings. For the data set with higher genuine scores, superior recognition performance is expected. The mean value of the high-quality matchings is 122.43, whereas that of the

mixed matchings is 75.73, and that of the low-quality matchings is 52.31. Thus, the data set with higher overall quality performs the best when two prints from the same finger, of the same subject, are matched. Correspondingly, the impostor scores are shown in Fig. 11(b), where a superior data set is expected to have lower impostor scores. The mean value of high-quality matchings is 9.29, whereas that of the mixed matchings is 10.74, and that of the low-quality matchings is 13.39. Again, the set with higher overall quality achieves the better performance when two prints from the same finger but of two different subjects are matched.

Based on the distributions of genuine and impostor scores, the ROC curves for high-, mixed-, and low-quality matchings are shown in Fig. 12. For high-quality matchings when the FAR is 0.01, the TAR is 0.986, while for mixed-quality matchings, the TAR is 0.975. For low-quality matchings, the TAR is 0.71. Hence, the higher-quality data set achieves the better recognition performance. Thus, the relationship between overall quality and recognition performance that holds for conventional 2D prints is also true for 3D unwrapped fingerprints.

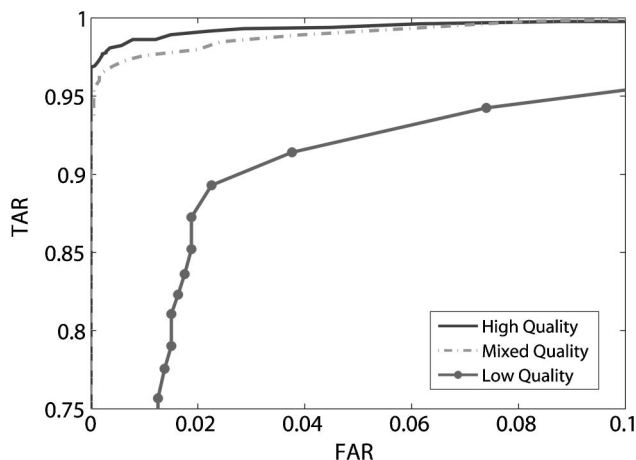


Fig. 12. ROC of the high-, mixed-, and low-quality matchings for 3D unwrapped fingerprints, TAR versus FAR.

5. Conclusions and Future Work

In this paper, a fit-sphere unwrapping algorithm was introduced for depth-detailed 3D fingerprints. By finding the best fit sphere, the algorithm unwraps the 3D prints where, since the detailed 3D information is known, the distortion caused by unwrapping is reduced by controlling the local distances between neighboring points. Detailed experimental analysis of the 3D unwrapped fingerprints were given and discussed in Section 4, which indicated a higher quality in local quality zone and minutiae detection of the 3D unwrapped prints versus traditional 2D ink rolled prints. The 3D unwrapped prints also achieved good recognition performance. Further, by classifying the 3D database into high- and low-quality sets, we demonstrated that the relationship between overall image quality and recognition performance of 3D

unwrapped prints is the same as the conventional 2D prints. Future work will include testing with a larger database, interoperability [35] between 3D and 2D fingerprints, and employment of multiple cameras [27,28] to obtain rolled-equivalent scans and higher depth precision.

This work is partially funded by Flashscan3D, LLC, Richardson, Texas, and the National Institute of Hometown Security, Somerset, Kentucky.

References

1. A. K. Jain, A. Ross, and S. Pankanti, "Biometrics: a tool for information security," *IEEE Trans. Inf. Forensics Secur.* **1**, 125–143 (2006).
2. S. Pankanti, S. Prabhakar, and A. K. Jain, "On the individuality of fingerprints," *IEEE Trans. Pattern Anal. Mach. Intell.* **24**, 1010–1025 (2002).
3. R. Cappelli, D. Maio, D. Maltoni, J. L. Wayman, and A. K. Jain, "Performance evaluation of fingerprint verification systems," *IEEE Trans. Pattern Anal. Mach. Intell.* **28**, 3–18 (2006).
4. A. Ross and A. K. Jain, "Information fusion in biometrics," *Pattern Recogn. Lett.* **24**, 2115–2125 (2003).
5. K. G. Larkin and P. A. Fletcher, "A coherent framework for fingerprint analysis: are fingerprints holograms?" *Opt. Express* **15** (2007).
6. J. C. Wu and C. L. Wilson, "Nonparametric analysis of fingerprint data," NISTIR 7226 (National Institute of Standards and Technology, 2005).
7. K. Tai, M. Kurita, and I. Fujieda, "Recognition of living fingers with a sensor based on scattered-light detection," *Appl. Opt.* **45**, 419–424 (2006).
8. S. Lin, K. M. Yemelyanov, J. E. N. Pugh, and N. Engheta, "Polarization-based and specular-reflection-based noncontact latent fingerprint imaging and lifting," *J. Opt. Soc. Am. A* **23**, 2137–2153 (2006).
9. J. C. Wu and M. D. Garris, "Nonparametric statistical data analysis of fingerprint minutiae exchange with two-finger fusion," NISTIR 7376 (National Institute of Standards and Technology, 2006).
10. A. Bal, A. M. El-saba, and M. S. Alam, "Improved fingerprint identification with supervised filtering enhancement," *Appl. Opt.* **44**, 647–654 (2005).
11. S. M. Rao, "Method for producing correct fingerprints," *Appl. Opt.* **47**, 25–29 (2008).
12. R. Shogenji, Y. Kitamura, K. Yamada, S. Miyatake, and J. Tanida, "Bimodal fingerprint capturing system based on compound-eye imaging module," *Appl. Opt.* **43**, 1355–1359 (2004).
13. R. Hashido, A. Suzuki, A. Iwata, T. Okmoto, Y. Satoh, and M. Inoue, "A capacitive fingerprint sensor chip using low-temperature poly-si TFTs on a glass substrate and a novel and unique sensing method," *IEEE J. Solid-State Circuits* **38**, 274–280 (2003).
14. S. Malassiotis, N. Aifanti, and M. G. Strinzis, "Personal authentication using 3-D finger geometry," *IEEE Trans. Inf. Forensics Secur.* **1**, 12–21 (2006).
15. N. Ratha and R. Bolle, *Automatic Fingerprint Recognition Systems* (Springer-Verlag 2004).
16. A. K. Jain and A. Ross, "Fingerprint mosaicking," in *ICASSP, IEEE International Conference on Acoustics, Speech, and Signal Processing—Proceedings* (IEEE, 2002), Vol. 4, pp. 4064–4067 (2002).
17. A. Ross, S. C. Dass, and A. K. Jain, "Estimating fingerprint deformation," in *Biometric Authentication* (Springer, 2004), pp. 249–255.
18. R. Rowe, S. Corcoran, K. Nixon, and R. Ostrom, "Multispectral imaging for biometrics," *Proc. SPIE* **5694**, 90–99 (2005).
19. G. Parziale, E. Diaz-Santana, and R. Hauke, "The Surround Imager™: a multi-camera touchless device to acquire 3D rolled-equivalent fingerprints," in *Advances in Biometrics*, Vol. 3832 of Lecture Notes in Computer Science (Springer, 2005), 244–250.
20. Y. Cheng and K. V. Larin, "In vivo two- and three-dimensional imaging of artificial and real fingerprints with optical coherence tomography," *IEEE Photon. Technol. Lett.* **19**, 1634–1636 (2007).
21. M. C. Potcoava and M. K. Kim, "Fingerprint biometry applications of digital holography and low-coherence interferography," *Appl. Opt.* **48** (2009).
22. Y. Chen, G. Parsiale, E. Diaz-Santana, and A. K. Jain, "3D touchless fingerprints: compatibility with legacy rolled images," in *2006 Biometrics Symposium: Special Session on Research at the Biometric Consortium Conference* (IEEE, 2006), pp. 1–6.
23. A. Fatehpuria, D. L. Lau, V. Yalla, and L. G. Hassebrook, "Performance analysis of three-dimensional ridge acquisition from live finger and palm surface scans," *Proc. SPIE* **6539**, 653904 (2007).
24. A. Fatehpuria, D. L. Lau, and L. G. Hassebrook, "Acquiring a 2-D rolled equivalent fingerprint image from a non-contact 3-D finger scan," *Proc. SPIE* **6202**, 62020C (2006).
25. S. Zhang and S. Yau, "Generic nonsinusoidal phase error correction for three-dimensional shape measurement using a digital video projector," *Appl. Opt.* **46**, 36–43 (2007).
26. J. Li, L. G. Hassebrook, and C. Guan, "Optimized two-frequency phase measuring profilometry light-sensor temporal-noise sensitivity," *J. Opt. Soc. Am. A* **20**, 106–115 (2003).
27. Y. Wang, K. Liu, D. L. Lau, and L. G. Hassebrook, "Multicamera phase measuring profilometry for accurate depth measurement," *Proc. SPIE* **6555**, 655509 (2007).
28. S. Zhang and S. Yau, "Absolute phase-assisted three-dimensional data registration for a dual-camera structured light system," *Appl. Opt.* **47**, 3134–3142 (2008).
29. V. Yalla and L. G. Hassebrook, "Very-high resolution 3D surface scanning using multi-frequency phase measuring profilometry," *Proc. SPIE* **5798**, 44–53 (2005).
30. S. Zhang, X. Li, and S. Yau, "Multilevel quality-guided phase unwrapping algorithm for real-time three-dimensional shape reconstruction," *Appl. Opt.* **46**, 50–57 (2007).
31. J. Wolberg, *Data Analysis Using the Method of Least Squares: Extracting the Most Information from Experiments* (Springer 2005).
32. E. Tabassi, C. L. Wilson, and C. I. Watson, "Fingerprint image quality," NISTIR 7151 (National Institute of Standards and Technology, 2004).
33. B. Kumar, M. Savvides, C. Xie, K. Venkataramani, J. Thomson, and A. Mahalanobis, "Biometric verification with correlation filters," *Appl. Opt.* **43**, 391–402 (2004).
34. Y. Cheng and K. V. Larin, "Artificial fingerprint recognition by using optical coherence tomography with autocorrelation analysis," *Appl. Opt.* **45**, 9238–9245 (2006).
35. A. Ross and R. Nadgir, "A calibration model for fingerprint sensor interoperability," *Proc. SPIE* **6202**, 62020B (2006).
36. S. D. Walter, "The partial area under the summary ROC curve," *Stat. Med.* **24**, 2025–2040 (2005).
37. J. C. Wu, "Studies of operational measurement of ROC curve on large fingerprint data sets using two-sample bootstrap," NISTIR 7449 (National Institute of Standards and Technology, 2007).